J Therm Spray Tech
https://doi.org/10.1007/s11666-024-01826-z

ORIGINAL RESEARCH ARTICLE

In Situ Measurement of Track Shape in Cold Spray Deposits

Scott E. Julien[1] · Nathaniel Hanson[2] · Joseph Lynch[2] · Samuel Boese[3] · Kirstyn Roberts[4] · Taşkin Padir[2] · Ozan C. Ozdemir[1] · Sinan Müftü[1]

Submitted: 19 December 2023 / in revised form: 19 July 2024 / Accepted: 6 August 2024

Abstract Cold spray is a material deposition technology with a high deposition rate and attractive material properties that has great interest for additive manufacturing (AM). Successfully cold spraying free-form parts that are close to their intended shape, however, requires knowing the fundamental shape of the sprayed track, so that a spray path can be planned that builds up a part from a progressively overlaid sequence of tracks. Several studies have measured track shape using ex situ or quasi-in situ approaches, but an in situ measurement approach has, to the authors' knowledge, not yet been reported. Furthermore, most studies characterize the track cross section as a symmetric Gaussian probability density function (PDF) with fixed shape parameters. The present study implements a novel in situ track shape measurement technique using a custom-built nozzle-tracking laser profilometry system. The shape of the track is recorded throughout the duration of a spray, allowing a comprehensive investigation of how the track shape evolves as the deposit is built up. A skewed track shape is observed—likely due to the side-injection design of the applicator used—and a skewed Gaussian PDF—a more generalized version of the standard Gaussian PDF—is fit to the track profile. The skewed Gaussian fit parameters are studied across two principal nozzle path parameters: nozzle traverse speed and step size. Empirical relationships between the fit parameters and the nozzle path parameters are derived, and a physics-based inverse relationship between nozzle speed and powder mass deposition rate is obtained. One of the fit parameters is shown to be an effective means of monitoring deposition efficiency during spraying. Overall, the approach presents a promising means of measuring track shape, in situ, as well as modeling it using a more general shape function.

Keywords additive manufacturing · cold spray · deposit shape · process monitoring · profilometry

Introduction

Cold spray is a solid-state material deposition process where powdered feedstock material is deposited by accelerating it to extremely high velocities and impinging it upon a surface. Metals and metal matrix composites (MMCs) have most commonly been sprayed using this technology, but polymers are also gaining interest (Ref 1, 2). To achieve the high velocities of the process, an accelerating gas (usually helium, nitrogen, or air) is heated and pressurized (typically to within ranges of 400-1100 °C and 1.0-6.0 MPa, respectively, for metals and MMCs) and then fed through a converging-diverging nozzle. The feedstock powder is supplied into this gas stream, where it achieves characteristic particle velocities within the range of 300-1200 m/s. Bonding is achieved by extreme plastic deformation of the particles upon impact with the substrate, which results in mechanical interlocking as well as material bonding from the high-pressure intimate contact between the particles and the impacted surface.

✉ Scott E. Julien
s.julien@northeastern.edu

[1] Department of Mechanical and Industrial Engineering, Northeastern University, 360 Huntington Ave, SN 334, Boston, MA 02115, USA

[2] Electrical and Computer Engineering, Northeastern University, Boston, MA 02115, USA

[3] Kostas Research Institute for Homeland Security at Northeastern University, Burlington, MA 01803, USA

[4] Eaton Corporation, Southfield, MI 48076, USA

Published online: 05 September 2024

A number of beneficial properties of the cold spray process make it attractive as a material deposition technology. Because the process occurs at relatively low temperatures as compared to melt-based processes—e.g., thermal spray, powder bed fusion, directed energy deposition, among others—it avoids deleterious thermally induced effects. This includes the formation of oxides and intermetallics, grain growth, phase changes, and tensile residual stresses (Ref 3, 4). Low and often compressive residual stresses are often imparted to cold spray deposits, and the original microstructure of the feedstock materials can be retained or even refined through the high-strain-rate cold working process (Ref 5-7). Furthermore, a wide variety of engineering metals (e.g., carbon steels, stainless steels and aluminum-, copper-, titanium-, zinc-, and tantalum-based alloys) and MMCs (e.g., alumina and chromium-, tungsten-, titanium-, and boron-carbide-based composites) can be sprayed (Ref 8).

For several decades, cold spray has been developed for applying coatings to surfaces and performing dimensional repair of damaged, worn, or corroded parts, in such industries as automotive, aerospace, and maritime (Ref 9). Recently, however—owing to its ability to produce dense deposits at a high material deposition rate with low defect density and relatively mild residual stresses—cold spray has also gained interest in the realm of additive manufacturing, as a means of producing near net-shape, free-form parts. For example, free-form aluminum, copper, bronze, and stainless steel parts for military and industrial applications have been produced (Ref 9).

The fundamental building block of a cold sprayed part is the track, a single line of material deposited by traversing the nozzle across a surface as the gas and feedstock material is sprayed. A two-dimensional layer of material is formed by depositing a sequence of tracks, side-by-side in an overlapping fashion. A full three-dimensional part is built by depositing a successive set of such layers on top of one another.

Because a three-dimensional cold sprayed part is, essentially, a superposition of sequentially sprayed tracks, properly planning the nozzle path for building a part requires knowledge of the cross-sectional shape of the track. The width, height, and cross-sectional shape of the track are affected by the spray parameters (e.g., feedstock material; accelerating gas type, temperature, and pressure; and nozzle geometry) and the nozzle path parameters (e.g., standoff distance, spray angle, and nozzle traverse speed). Once the fundamental shape of the track is characterized—as well as its relationship to the spray and nozzle path parameters—modeling tools can be developed that simulate the track-by-track buildup of a part. This enables the spraying process performed virtually, prior to performing an actual spray, allowing the nozzle path to be optimized without the need to perform costly parametric spray studies. Furthermore, modern machine learning algorithms can be used to facilitate the optimization process (Ref 10, 11).

Several different measurement methodologies have been used in the literature to measure the cross-sectional shape of the track in cold spray and thermal spray technologies, in general physical cross-sectioning (Ref 3, 12, 13), contact probing (Ref 14), chromatic confocal or laser interferometric microscopy (Ref 15, 16), triangulated laser profilometry (Ref 16-18) and optical coherence tomography (OCT) (Ref 19). Kotoban et al. (Ref 12), for example, characterized the height and width of single tracks of 316L stainless steel (SS) by physically cross-sectioning the deposits after spraying, then measuring the dimensions of the cross sections. Fasching et al. (Ref 14) performed contact probing on single tracks and layers of plasma-sprayed ceramic coatings, by using a contact depth probe affixed to an end mill to conduct evenly spaced surface height measurements. Chen et al. (Ref 15) used chromatic confocal or laser interferometric microscopy (the exact technique was not specified) to measure the cross-sectional profiles of single tracks and single layers of aluminum (Al) 5056 deposits. Ikeuchi et al. (Ref 16) and Wu et al. (Ref 17) used triangulated laser profilometry to measure the cross-sectional profiles of Grade-2 titanium (Ti) and Al 7075, deposited at different spray angles, nozzle traverse speeds, and standoff distances.

All of the above studies performed the shape measurements ex post facto (after spraying), due to the practical difficulties of implementing a measurement instrument, in situ. Such constraints include high gas velocities and temperatures, limited space in the vicinity of the nozzle and robot end effector, and risk of contamination by the feedstock powder. Cojucaru et al. (Ref 19) took a quasi-in situ approach wherein the deposit shape was periodically measured during spraying using OCT. The sample was mounted to a robot arm, and, periodically during spraying, the sample was moved from the spray area to a nearby OCT scanner for shape measurement.

A number of studies have been conducted to characterize the relationship between the track shape and the spray and nozzle path parameters. Kotoban, et al. (Ref 12) studied the effect of nozzle traverse speed on track height and deposition efficiency (DE) of their 316 L SS deposits and found that although track height showed an expected increase with decreasing nozzle speed, DE decreased, due to the increasingly sloped sides of the taller tracks at slower speeds. In sprays of grade-2 Ti, Ikeuchi et al. (Ref 16) found a significant inverse relationship between nozzle traverse speed and track height for speeds from 25 to 200 mm/s, but a weak relationship between track height/width and standoff distance for distances in the range of 30 and 50 mm. Decreasing spray angle from 90° to 45° was found

to increase track asymmetry but decrease DE. Chen et al. (Ref 15) and Wu et al. (Ref 17) made the same observations on traverse speed and spray angle for their range spray parameters and materials, respectively. Wu et al. (Ref 17), however, observed a clear variation in DE with standoff distance (over a range of 10-45 mm), with a maximum occurring at an intermediate distance. This observation has been confirmed by others, as well (Ref 20).

Several studies have modeled the deposit buildup process from the track cross-sectional shape. Cai et al. (Ref 20) developed a two-dimensional (2D) model that superimposed the Gaussian cross sections of adjacent tracks to model the buildup of the deposit cross section. Jeandin et al. (Ref 13) developed a 2D model that treated any arbitrary measured track profile as a series of equally spaced discrete height points joined by line segments, which they verified against Al 2024 sprays. Chen et al. (Ref 15) extended the model by Cai et al. (Ref 20) to include the effect of non-normal spray angle. Relationships between nozzle path parameters—such as nozzle speed and standoff distance—and the Gaussian profile parameters were incorporated into the model through empirically derived relationships. Loss in deposition efficiency (DE) due to spraying on sloped surfaces was also taken into account via a functional relationship between DE and underlying surface angle, θ, which was measured empirically.

Several groups have also developed three-dimensional (3D) models of the deposition process. Jeandin et al. (Ref 13) extended their 2D discretization approach to three dimensions (3D) by juxtaposing the 2D cross sections longitudinally along the spray path. Wu et al. (Ref 17) developed a 3D model based upon the superposition of discrete axisymmetric Gaussian "piles" of deposit along the spray path. The model was able to account for the effects of shadowing substrate non-uniformity, and they used it to optimize the spray parameters (nozzle angle and spray distance) for spraying tall vertical walls (Ref 18). Tzinava et al. (Ref 21) developed an algorithm for computing the surface profile of a deposit sprayed over a triangulated surface (e.g., a part from an STL file), using a Gaussian profile calibrated from a set of experimental sprays.

Most of the above models assume that track or spot cross-sectional base shape is a symmetric (2D) or axisymmetric (3D) Gaussian distribution that superimposes consistently during the spray process (Ref 12, 15, 17, 18, 20, 21). This is attributed to the fact that, in the particle-gas jet plume as it exists the nozzle, the number of particles, the average particle size, and particle and gas velocity all decrease from the center of the plume toward the outer edges in a Gaussian manner. However, Ikeuchi et al. (Ref 16, 22) demonstrated that an artificial neural network (ANN) can be used to model the relationship between 2D track profile and the nozzle path parameters spray angle, nozzle traverse speed, and standoff distance. It must be noted, however, that this was for a specific feedstock material and set of spray parameters.

While the use of ML algorithms for learning the relationships between the spray parameters and deposit shape is virtually limitless in its flexibility, in order to encompass the many combinations of materials and spray parameters that are used in cold spray, the use of such an approach requires a significantly large range of training parameters. The use of an analytical profile shape, such as a Gaussian distribution with just two or three shape parameters, can potentially mitigate this added complexity by allowing general relationships between the shape parameters and the materials/spray parameters to be gleaned from a smaller set of representative experiments. Furthermore, despite the advancements in track shape measurement mentioned earlier, to the authors' knowledge no study has yet reported the measurement of track shape, in situ, in the cold spray literature. Significant advantage can be obtained by measuring deposit shape in situ, by enabling the entire evolution of the deposit shape to be studied. Finally, to the authors' knowledge, no studies have yet thoroughly assessed whether the commonly used Gaussian profile in analytical models of profile geometry is consistent as a deposit builds up—particularly as an increasing number of layers or highly sloped edges are accumulated.

In the present work, rather than fitting track cross section with a conventional Gaussian distribution, the efficacy of fitting the track shape with a skewed Gaussian distribution that can accommodate an asymmetric track cross section was investigated. As will be discussed later, a skewed Gaussian distribution is a more generalized version of a Gaussian distribution that encompasses the standard Gaussian distribution as a special case. Therefore, it can represent the common case in which the track is symmetric and Gaussian in profile, while it also possesses the flexibility to represent the case in which the track shape is asymmetric.

In the present study, a series of basic, rectangular, rastered deposits were sprayed using several variations of nozzle speed and step size. During spraying, the buildup of the deposits was recorded, track-by-track, using a custom-built, in situ laser profilometry system. The laser profilometry system was used to record the shape of rastered deposits as they were being sprayed, and the cross-sectional shape of the track was recorded during the entire duration of the sprays. After recording the shape data from the sprays, a skewed Gaussian fit was applied to the track profiles, and the corresponding fit parameters were computed on a track-by-track basis for the evolving deposits. Connections between fit parameters and deposit shape quality were investigated. Relationships between fit

parameters and nozzle path variables were also extracted from the data.

Materials and Methods

Spraying

Aluminum 6061 alloy (Al 6061) was chosen as the feedstock powder because of its common use in cold spray applications, its ready availability, and its good sprayability. Military specification (Mil-DTL-32495C, Amendment 2 (Ref 23)) Al 6061 powder was acquired from Valimet® (Stockton, CA, USA). Particle size distribution was characterized using light microscopy and image analysis using custom-written MATLAB® (Mathworks, Natick, MA, USA) code (Ref 24). For substrate material, Al 6061-T651 was selected, and plates 150 × 150 × 6.35 mm were acquired with an industrial mirror polish (McMaster-Carr®, Elmhurst, IL, USA). The latter ensured a smooth surface, such that the substrate could be easily distinguished from the deposit during the profilometry measurements. Because interfacial bond strength was not a concern for the present study, no pre-spray surface roughening through grit-blasting, machining, or other operation was performed, so as to preserve the polished surface finish. Prior to spraying, the substrates were simply wiped with 100% ethyl alcohol.

Spraying was conducted using a VRC® Gen III Max (Box Elder, SD, USA) cold spray system, equipped with a Fanuc® M-710iC (Rochester Hills, MI, USA) industrial robot arm and a rotary positioning table. The spray parameters are listed in Table 1. To ensure that spray conditions did not significantly change during sprays, consistency between particle velocities at the start and end of each spray was confirmed by performing laser tracking particle velocimetry measurements using an Oseir® HiWatch HR (Tampere, Finland) system.

Table 1 Spray parameters used in the present study

Spraying system	VRC Gen III Max®
Powder type	Valimet® Al 6061, Mil-DTL-32495C, Amend. 2, 230-mesh
Particle size distribution	D10: 19 μm, D50: 34 μm, D90: 51 μm
Powder feed rate	8.5 g/min
Gas type	Helium
Gas pressure	3.5 MPa
Gas temperature	400°C
Nozzle material	polybenzimidazole (PBI)
Nozzle throat length	2.7 mm
Nozzle diverging length	153.2 mm
Nozzle throat diameter	1.75 mm
Nozzle exit diameter	4.85 mm
Nozzle standoff distance	25.4 mm
Nozzle traverse speed	25, 50, and 100 mm/s
Rastering step size	0.5, 1.0, and 1.5 mm

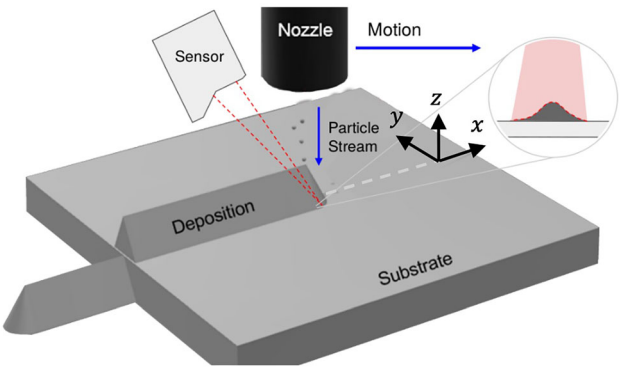

Fig. 1 Operating principle of the in situ profilometer assembly. Figure adapted and reprinted from (Ref 25), with permission from the author

In Situ Profilometry

To measure the deposit profile in situ a profilometer assembly was custom-built to mount behind the nozzle and measure the profile of each track as it was deposited (Fig. 1 and 2a). The assembly consists of a Keyence® LJ-V7060 (Itasca, IL, USA) laser profilometer mounted to a pivoting assembly around the nozzle (Fig. 2b). Custom control code was written in the open-source robot control software, ROS (Robot Operating System®) to track the direction of the nozzle and maintain the profilometer position behind it during spraying (Ref 25). The profilometer used a 16-mm wide laser line cast on the substrate 38 mm (1.5 in.) behind the nozzle. In order to minimize vibration of the profilometer and consequent noise in the track profile readings, the profilometer assembly was mounted on a ball bearing with tight radial and axial play. Furthermore, so as to prevent the high-temperature nozzle gases from damaging the profilometer—as well as prevent the profilometer from interfering in the gas dynamics of the spray plume—it was positioned approximately 35 mm above and 30 away from the target spray spot on the substrate.

The width of the laser line consisted of 160 evenly spaced points, yielding a width (local y-coordinate) resolution of 100 μm. At each of these points, a corresponding height (local z-coordinate) value was measured, with a vertical resolution of 0.4 μm. The laser profilometer scanned the surface at an average rate of 110 scans/sec, resulting in a longitudinal (local x-coordinate) resolution that varied with nozzle traverse speed: 225 μm at 25 mm/s,

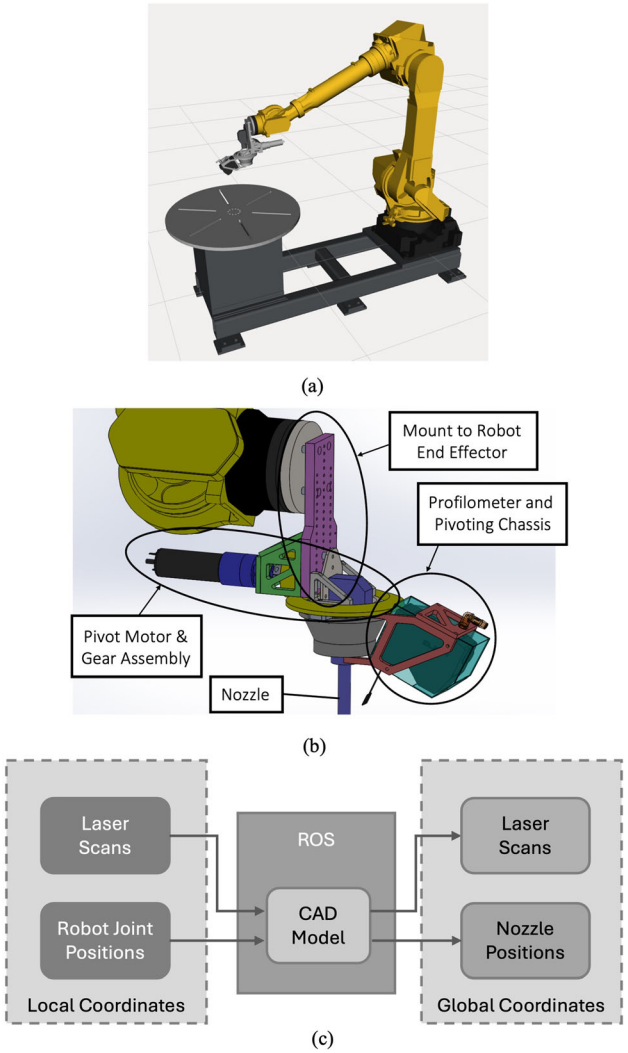

Fig. 2 (a) CAD replica of the robot-profilometer-spray table system in ROS. (b) Closeup view of the in situ profilometer assembly. (c) Data flow of the in situ profilometry system. (a) and (b) adapted and reprinted from (Ref 25), with permission from the author

450 µm at 50 mm/s, and 900 µm at 100 mm/s. To verify the accuracy of the profilometer, a scan of a representative deposit was compared to a corresponding scan of the same deposit using a 3D coordinate measurement machine ("CMM", Creaform® MetraSCAN BLACK, Lévis, Quebec, Canada) which had a resolution along all axes of 25 µm.

In order to track the position of the nozzle during spraying—as well as transform the laser scans from local coordinates relative to the scanner to global coordinates relative to the spray table—the ROS configuration included an exact CAD replica of robot/profilometer assembly (Fig. 2b). During spraying, the positions of the robot joint actuators were acquired from the robot controller, in real time, and the CAD replica was used to perform the coordinate transformations needed to determine the real-time global positions of the laser scans and nozzle (Fig. 2c). The real-time global nozzle positions were, in turn, used to determine the real-time traverse speed of the nozzle.

Spray Pattern

In order to determine how fundamental deposit shape builds up to produce more complex shapes, deposits were sprayed using a uni-directional raster pattern, and the deposit profile was recorded on a track-by-track basis via the in situ profilometer. So as to determine the relationship between deposit shape and spray parameters, nozzle traverse speed and step size (hereafter, defined as, v_n and d_s, respectively) were varied over a range of values. For v_n, values ranging from 100 to 250 mm/s are typical for thin deposits (Ref 15, 18, 26), while values ranging from 10 to 100 mm/s are typical for thick deposits (Ref 15, 18, 27). In the present study, a moderate range of 25 to 100 mm/s was chosen, and values of 25, 50, and 100 mm/s were adopted. For d_s, a value between 0.5 and 1 mm is typical for sprays (Ref 9), but larger values (e.g., 2 mm) are sometimes used (Ref 26). In the present study, values of 0.5, 1.0, and 1.5 mm were used. The width of each track was approximately 6 mm (c.f. Section 2.4), resulting in overlays between adjacent tracks of approximately 92%, 83%, and 75%, respectively. So as to produce deposits with a maximum width of 25 mm, a fixed width of 16 contiguous tracks was selected for all the deposits (which produces deposits of 24-mm width for the 1.5-mm step size).

For each (v_n, d_s) combination, a different thickness per layer is produced. So as to maintain some level of consistency between overall deposit heights, a specific number of layers, N, was sprayed for each nozzle speed. The value of N was defined as the number of layers required to produce a deposit approximately 3-5 mm in thickness for a step size of 1.0 mm. (While such a thickness was not required to measure the shape in the present study, this was the approximate minimum thickness required to obtain residual stress profiles through the thickness of the deposits using x-ray diffraction. The results of these measurements will be presented in a later paper.) The thickness per layer at each (v_n, d_s) combination was computed using total thickness data collected from previous sprays in the authors' cold spray laboratory using the same materials and spray parameters. The estimates for these thicknesses are presented in Table 6 of the Supplementary Information (SI). Based upon these, N was set at 2, 4, and 8 layers, for the 25-, 50-, and 100-mm/s deposits, respectively.

A fixed nozzle height will yield a gradually decreasing standoff distance from the top of the deposit as it builds up in thickness. This can cause changes in deposition efficiency and track shape. In order to prevent this effect, after

Table 2 Combinations of nozzle path parameters used to spray the nine deposits in the present study

Nozzle speed, mm/s	Step size, mm	No. of layers
25	0.5	2
25	1.0	2
25	1.5	2
50	0.5	4
50	1.0	4
50	1.5	4
100	0.5	8
100	1.0	8
100	1.5	8

each layer was sprayed, the nozzle was stepped upward by an increment, Δz, equal to the layer thickness.

A key parameter that was not studied in the present work was nozzle standoff distance (SoD). It was set at a fixed value of 25 mm—typical for raster sprays (Ref 18, 27, 28). Preliminary sprays by the authors for SoD values varied from 20 to 50 mm (not reported here) had shown a negligible effect of SoD on track shape. This has also been reported in the literature when SoD is varied over a small range (Ref 16). However, when varied over larger ranges (e.g., 10-200 mm), SoD has been reported to influence the velocity distribution of the particles in the jet plume (Ref 29). This has an effect on overall deposition efficiency (Ref 17, 29-31), and it can, in principle, also affect the shape of the track, especially if the velocity of some portion of the particles in the plume falls below the critical velocity. Therefore, although SoD was not studied in the present work, a thorough investigation of its effect over a broad range of values is warranted in future work.

Based on the above development, nine deposits were sprayed, using the nozzle path parameter combinations listed in Table 2.

Track Profile Extraction

To assess the evolution of the track profile shape during the spraying process, a representative profile for each track was sought. From the profilometry data, each laser scan consisted of a set of local width, y, and height, z, coordinates, (y_i, z_i), evenly spaced in y by the width resolution of $\Delta y_i = 100$ μm. Along the longitudinal (local x) direction, each track consisted of a set of scans whose total number along the track depended upon the nozzle speed. For example, Fig. 3(a) shows all of the scans for the 25-mm/s, 0.5-mm, two-layer deposit.

Note, here, that the scans where the nozzle was either accelerating or decelerating at the ends of the track are

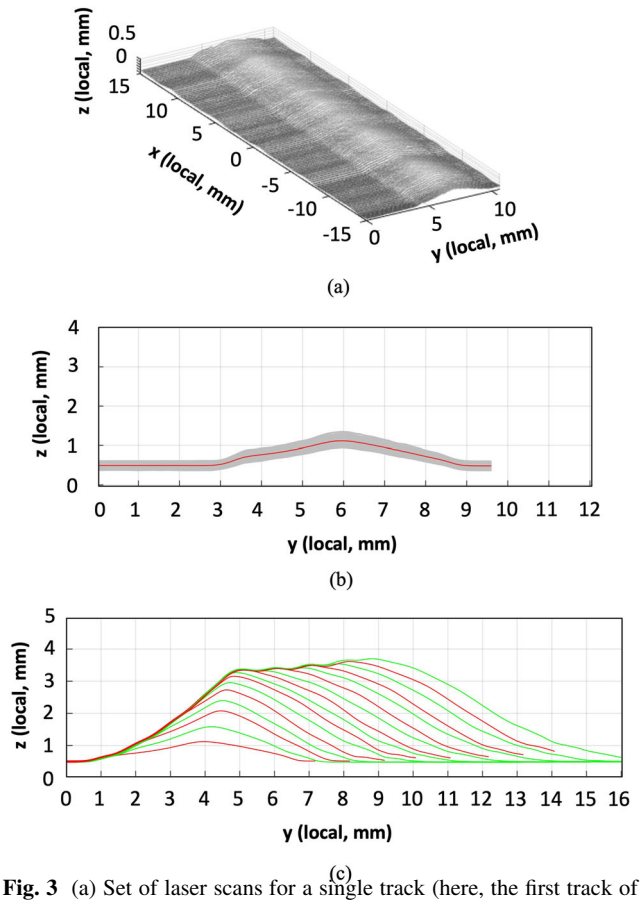

Fig. 3 (a) Set of laser scans for a single track (here, the first track of the 25-mm/s, 0.5-mm, two-layer deposit). (b) Cross-sectional view of (a), showing scans projected onto y–z plane (gray curves) and mean of scans along deposit length (red curve). (c) Track-by-track buildup of the first layer of the deposit. Red and green colors correspond to the mean profiles where the nozzle is moving toward and away from the viewer, respectively. First (lower-left red) track corresponds to the red mean curve in (b)

omitted from the data and subsequent analysis. Only the scans along the central portion of the track length, where the nozzle was traveling at full, nominal speed (25, 50, or 100 mm/s), were analyzed. The length of this portion varied inversely with nozzle speed, due to the fact that, at higher nozzle speeds, the distance required to accelerate and decelerate to/from full nominal speed at the ends of the deposit was longer. For 25 mm/s, the distance over which the nozzle was accelerating/decelerating was approximately 25 mm on either end of the deposit, with the central portion over which the nozzle was traveling at full, nominal speed being 50 mm (50% of the total 100-mm deposit length). For the 50 mm/s and 100 mm/s deposits, the accelerating/decelerating portions were approximately 28 and 40 mm at either end, respectively, with the central portion consisting of approximately 44 and 20 mm.

Because of vibration of the profilometer during nozzle traversal, as well as local variation in the deposit profile, some shape variation in the scans was present. In Fig. 3(a),

this is visible as unevenness of the track top surface. Figure 3(b) shows a cross-sectional view of Fig. 3(a), where the gray region is all of the scans from Fig. 3(a) projected onto the y–z plane. The unevenness of the top surface is visible in the fact that the scans do not all coincide but cover a finite region (approximately ±0.2mm in the vertical direction). In order to obtain a single representative profile of a given track, the mean of the scans was taken along the length of the track. The result was a set of mean datapoints, $(\overline{y}_i, \overline{z}_i)$, evenly spaced by $\Delta\overline{y}_i = 100$ μm (red curve in Fig. 3b). In order to obtain a track-by-track depiction of the buildup of the entire deposit, the above process was repeated for all of the tracks.

Skewed Gaussian Distribution Fitting

A standard Gaussian probability density function (PDF), when cast in the coordinates of the present problem (c.f. Fig. 3), can be represented as follows:

$$z(y) = \frac{a}{\sqrt{2\pi}\sigma}\exp\left[-\left(\frac{y-\mu}{\sqrt{2}\sigma}\right)^2\right] \quad \text{(Eq 1)}$$

where y is the lateral in-plane (width) coordinate, z is the out-of-plane (height) coordinate, μ is the mean; σ is the standard deviation; and a is an amplitude parameter. Note that μ represents the location of the center of the distribution, and a represents the area under the distribution. (The latter can be verified by integrating Eq 1 over y, which is demonstrated in Appendix 1). The standard deviation, σ, is a measure of the width (or "spread") of the distribution, where approximately 68.2% of the overall area under the distribution falls within $\pm\sigma$ about the mean, 95.4% falls within $\pm 2\sigma$, and 99.7% falls within $\pm 3\sigma$. Thus, although a Gaussian distribution, by definition, spans the interval $(-\infty, \infty)$, the "width" of a given distribution is often approximated to be between 4σ and 6σ (95.4% to 99.7%, respectively).

For a set of n mean profile datapoints (y_i, z_i) evenly spaced by Δy_i in the y-direction (where, without loss of generality, the bar superscript in Section 2.4 has been dropped for simplicity), the parameters a, μ, and σ can be estimated using expressions derived using the method of maximum likelihood (Ref 32):

$$a = \sum_{i=1}^{n} z_i \Delta y_i \quad \text{(Eq 2a)}$$

$$\mu = \frac{1}{a}\sum_{i=1}^{n} y_i z_i \Delta y_i \quad \text{(Eq 2b)}$$

$$\sigma^2 = \frac{1}{a}\sum_{i=1}^{n} (y_i - \mu)^2 z_i \Delta y_i \quad \text{(Eq 2c)}$$

Note that, here, each (y_i, z_i) pair can also be thought of as the abscissa, ordinate pair of a single bar in a histogram, and Δy_i can be thought of as the bin width. Using this conceptualization, the product $z_i \Delta y_i$ can be thought of as representing the number of individuals in a given bin, and the expressions for μ and σ subsequently reduce to the well-known formulae $\mu = \frac{1}{n}\sum_{i=1}^{n} y_i$ and $\sigma^2 = \frac{1}{n}\sum_{i=1}^{n}(y_i - \mu)^2$.

Equations 2a through 2c give a straightforward, analytical means of obtaining the best-fitting standard Gaussian distribution to each of the mean track profiles. However, because of the skewed nature of the track cross sections in the present study, a standard symmetric Gaussian distribution is not the most suitable. In the present work, it is proposed that a skewed Gaussian fit can more universally represent the shape of a track cross section than the standard Gaussian distribution most commonly used in deposit shape simulation tools reported in the literature. O'Hagan and Leonard (Ref 33) and Azzalini (Ref 34) proposed a skewed version of the Gaussian PDF, which can be represented by:

$$z(y) = \frac{A}{\sqrt{2\pi}\omega}\exp\left[-\left(\frac{y-\xi}{\sqrt{2}\omega}\right)^2\right]\left[1 + \operatorname{erf}\left(\alpha\frac{y-\xi}{\sqrt{2}\omega}\right)\right] \quad \text{(Eq 3)}$$

where ξ is the so-called "location" parameter; ω is the "spread" parameter, A is the amplitude parameter, and α is a parameter representing the degree of skewness of the distribution. Note that ξ, ω, and A are analogous to μ, σ, and a, respectively, for the standard Gaussian distribution: ξ is the approximate location of the center of the distribution; ω is an approximate measure of the width; and A is the approximate overall cross-sectional area. For the skew parameter, when $\alpha > 0$, Eq 3 is skewed positively (with the longer tail to the right, and the narrower tail to the left), and when $\alpha < 0$, Eq 3 is skewed negatively (with the longer tail to the left and the narrower tail to the right). When $\alpha = 0$, Eq 3 is symmetric and reduces to Eq 1 (after substituting σ for ω, μ for ξ, and a for A). Therefore, the standard Gaussian distribution is a special case of the skewed Gaussian distribution. Note, in the above, that ξ, ω, and A only represent the geometric center, first standard deviation, and cross-sectional area for this special case. For nonzero α, the center of the distribution does not exactly coincide with $y = \xi$; the 68%, 95%, and 99% percentiles of overall area do not fall exactly within 2ω, 4ω, and 6ω about ξ, respectively; and the cross-sectional area is not exactly A (see Appendix 2). Nonetheless, for sufficiently small values of α—such as the relatively small values encountered in the present study (generally, $\alpha < 4.5$, c.f. "Skew Parameter" Section)—the above parameters are reasonable approximations of these shape properties.

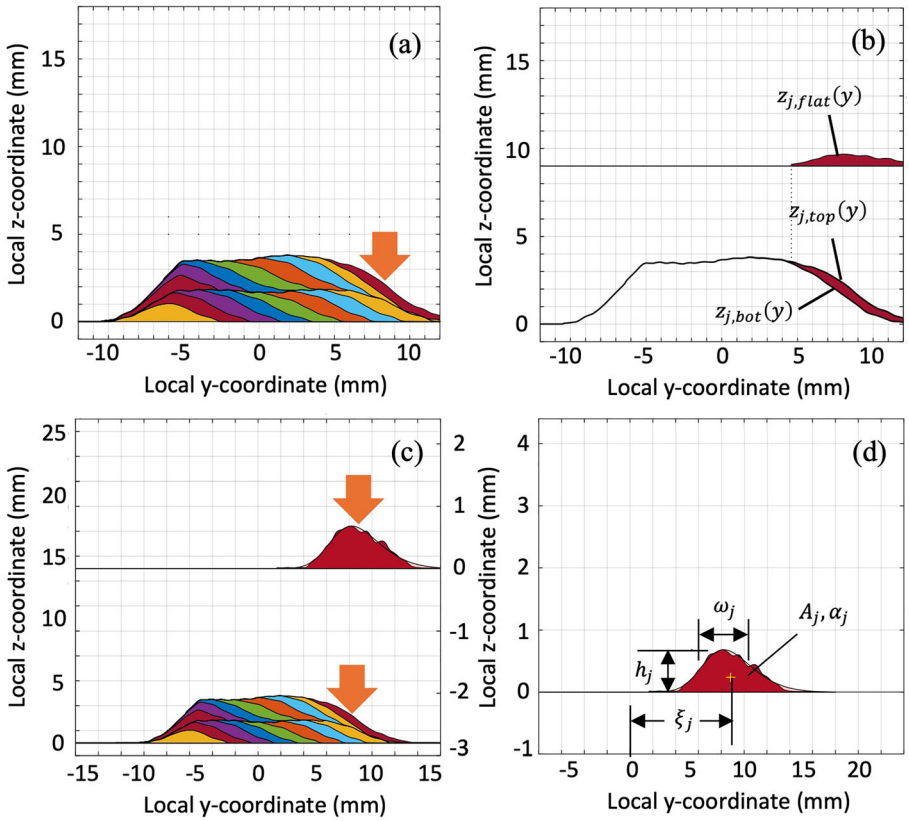

Fig. 4 Fitting each track of a deposit (here, the 25-mm/s, 1.0-mm, 2-layer deposit) with the skewed Gaussian probability density function of Eq 3: (a) original shape of the last track; (b) re-expressing the track as having been sprayed on a flat surface; (c) applying the skewed Gaussian fit; (d) computing the geometry and fit parameters, A_j, h_j, ω_j, and α_j. (Note that the z-scale of $z_{j,flat}(y)$ in Fig. 4(b) is exaggerated in Fig. 4(c) and (d) for better clarity)

Closed-form expressions analogous to Eq. 2 cannot be obtained for the skewed Gaussian distribution (Ref 32). In order to obtain estimates of A, ξ, ω, and α, for a given set of datapoints, it is, therefore, necessary to resort to numerical techniques. Two options are: (i) to perform a numerical application of the maximum likelihood method, or (ii) to perform a nonlinear least-squares regression of Eq 3 to the scan data. For option (i), custom code must be written to iteratively adjust each of the shape parameters, one at a time, until the likelihood function for (3) is maximized. For option (ii), the least-squares regression can be performed by built-in functions in common numerical analysis software such as MATLAB. In the present work, because of its greater simplicity, the latter was performed. A relatively straightforward MATLAB script was used to perform the least-squares regression for each mean track profile.

Here, it is important to note that, in the present work, the fitting was done for every other track, rather than every track. This was because there was a slight misalignment of the profilometer in its mount, which caused a slight misalignment between the scans in the positive-x versus the negative-x direction (red and green directions, respectively, in Fig. 3c). As some slight sensor misalignment is inherent when mounting the profilometer in its holder (and, for that matter, any sensor in its fixture), future versions of the system will have a software algorithm for compensating for the misalignment. As of this study, however, such a feature was not yet included in the system, and only the scans in one direction (here, the negative-x direction) were analyzed. As a result of all of this, each of the laser scans presented herein actually represents the deposition of two consecutive tracks. Hence, while the term "track" is used to refer to them, this fact must be born in mind.

In order to fit each track with Eq 3, it was first necessary to re-depict it as if it were sprayed on a flat surface. The process is illustrated in Fig. 4 for the last track in the 25-mm/s, 1.0-mm, 2-layer deposit. The profile of the surface onto which the track was sprayed was subtracted from the profile of the track, itself. Mathematically, this can be represented for arbitrary track, j, by

$$z_{j,\mathrm{flat}}(y) = z_{j,\mathrm{top}}(y) - z_{j,\mathrm{bot}}(y) \qquad \text{(Eq 4)}$$

where $z_{j,\mathrm{top}}(y)$ and $z_{j,\mathrm{bot}}(y)$ are the respective contours of the top and bottom surfaces of the track cross section, and $z_{j,\mathrm{flat}}(y)$ is the resulting top-surface contour of the track as if sprayed on a flat surface (c.f. Fig. 4b). The nonlinear least-squares regression of Eq 3 was then performed on $z_{j,\mathrm{flat}}(y)$ (Fig. 4c). After performing the fit, the best-fit parameters, A_j, ω_j, α_j, and ξ_j—along with the peak height, h_j, of the fit—were obtained (Fig. 4d). In Fig. 5(a) through Fig. 5(d), A_j, ω_j, α_j, and h_j were plotted together for all the tracks in the deposit, respectively. (Note that although ξ_j was

computed, it is not presented here because it, essentially, is simply the location of the track with respect to the origin of the deposit local coordinates. Therefore, it gives very little information about the shape of the track, which is of primary interest, here.) The process above was performed for each of the nine deposits in the present study, allowing any trends among the fit parameters to be observed, from track to track and layer to layer. In addition, the overall mean of each of these parameters was computed for each deposit and compared to v_n and d_s, to determine if any relationships existed between them.

Results and Discussion

Figure 6 shows the array of nine deposits sprayed in the present study corresponding to the nozzle path parameters specified in Table 2. In the sections that follow, the qualitative shape of the deposits is first discussed, followed by trends in the overall deposit means of the skewed Gaussian fit parameters, A, h, ω, and α. (Note that the subscript, j, representing each track number is hereafter dropped for brevity.) To provide conciseness to the below discussion,

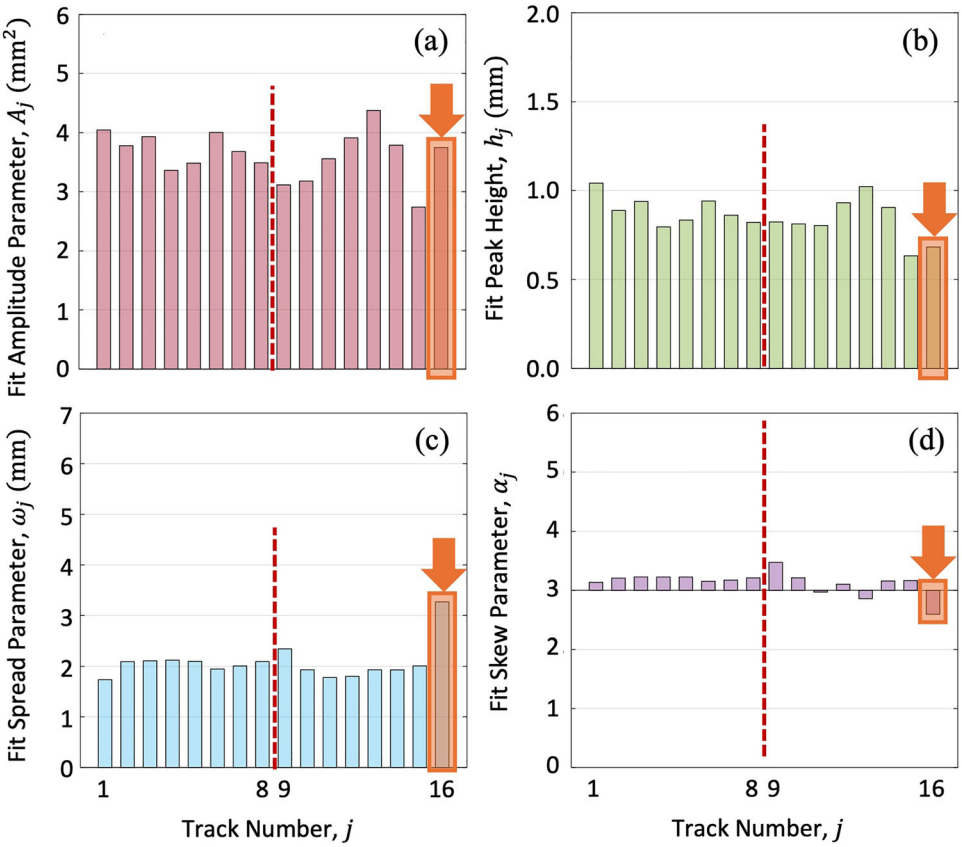

Fig. 5 Fit parameters for each track, j, from the skewed Gaussian fits in Fig. 4: (a) amplitude parameters, A_j, (b) peak heights, h_j, (c) spread parameters, ω_j, and (d) skew parameters, α_j. Orange highlighted bars correspond to the track discussed in Fig. 4. Vertical dashed red lines indicate transitions between layers

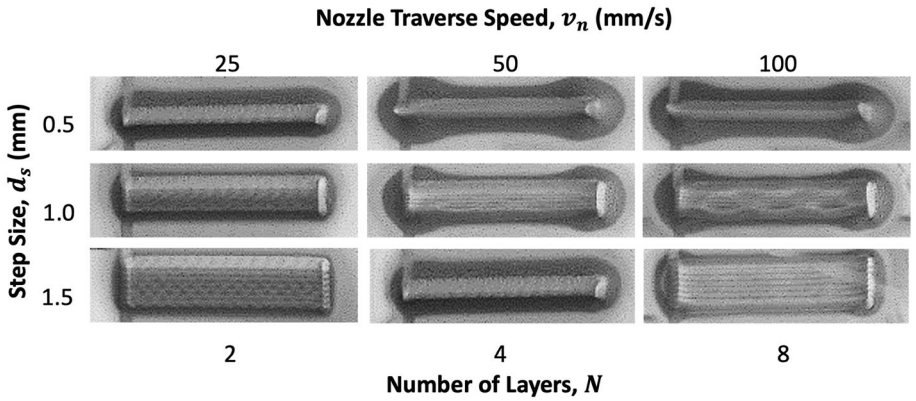

Fig. 6 Array of deposits sprayed in the present study

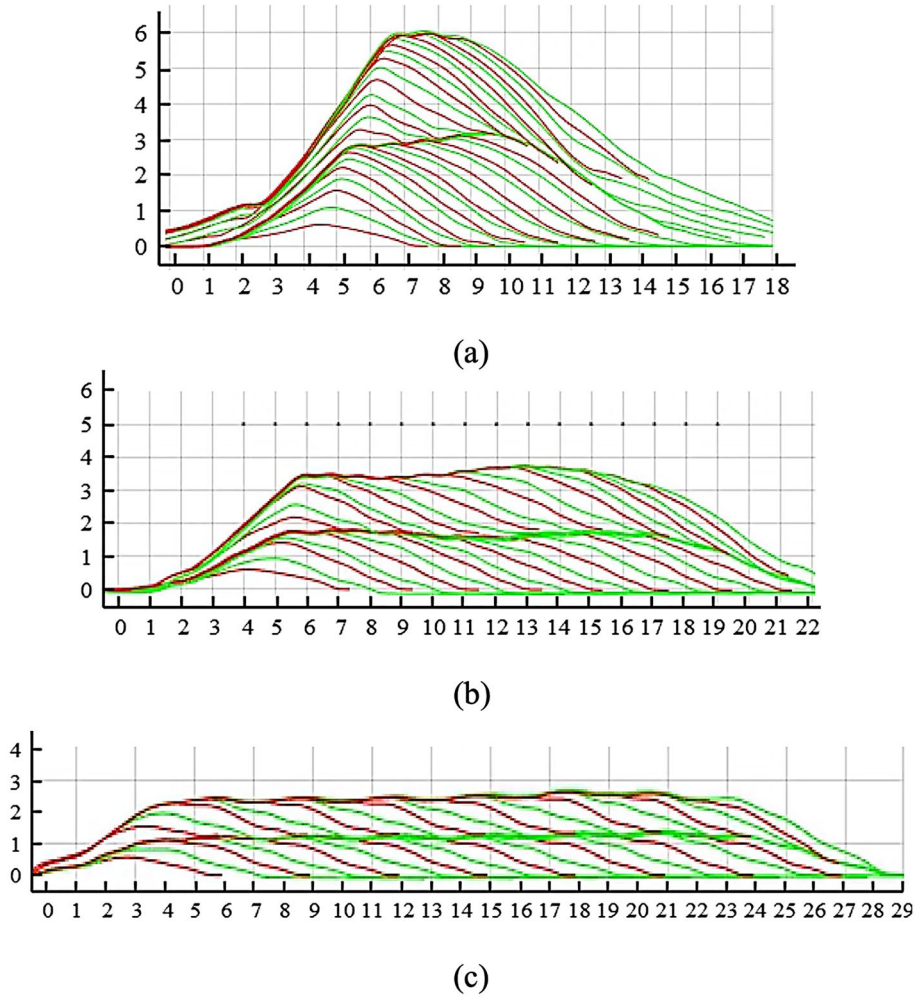

Fig. 7 Mean laser scan profiles of all the 25-mm/s deposits: (a) 0.5-mm step size, (b) 1.0-mm step size, (c) 1.5-mm step size. (Red and green colors correspond to the mean profiles where the nozzle is moving toward and away from the viewer (−x and + x directions), respectively. Dimensions are in millimeters)

track-by-track values of the fit parameters—upon which the deposit means are based—are presented in the SI.

Profilometer Scans

Figure 7 shows the track-by-track profiles of all the 25-mm/s deposits, obtained by averaging along each track as described in Section 2.4. Corresponding profiles were also obtained for the 50- and 100-mm/s deposits but are not presented here.

Qualitative Shape

Figure 8 presents the shapes of the nine deposits analyzed in the present study. Again, each track, here, represents two consecutive tracks in Fig. 7 (the green (−x) tracks). The tracks are color-coded to facilitate differentiation. The black dots above the deposits correspond to horizontal positions of the nozzle. (Note that they do not represent the actual vertical positions, which extend beyond the upper limit of the vertical axes. For visualization, they have been artificially shifted downward, vertically.) A number of qualitative observations can be made from this figure. Firstly, there is a clear tradeoff between overall deposit height and width as a result of changing the step size, d_s. As d_s is increased (from left-to-right in the figure), overall deposit height decreases and width increases. However, for a given nozzle speed, v_n, close inspection of the tracks reveals that the dimensions of each individual track do not change. Rather, as d_s is increased, there is a reduction of overlap between adjacent tracks, causing the decrease in height and increase in width of the overall deposit. This observation is commonly reported in the literature (Ref 13, 15, 18, 20, 35).

There is also a relationship between v_n and the number of layers required to produce the same deposit height. As v_n is increased (from top-to-bottom in Fig. 8), the cross-sectional area and height per track decrease, reducing the thickness per layer. This observation is commented on in greater detail in "Amplitude Parameter" and "Peak

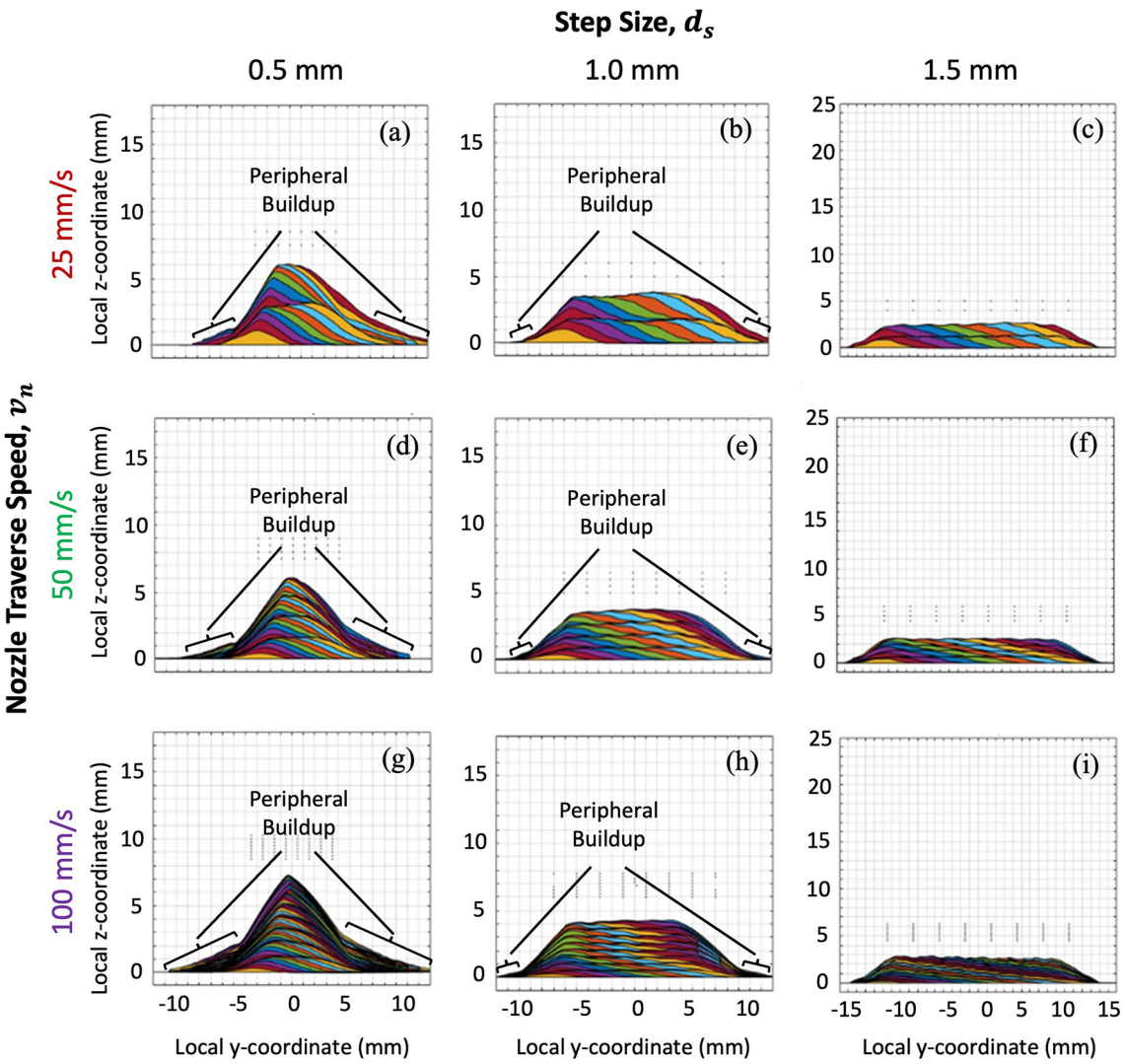

Fig. 8 Cross-sectional profiles of the nine deposits in the present study (Fig. 6). Tracks are color-coded to facilitate differentiation. Black dots above the deposits correspond to relative horizontal positions of the nozzle

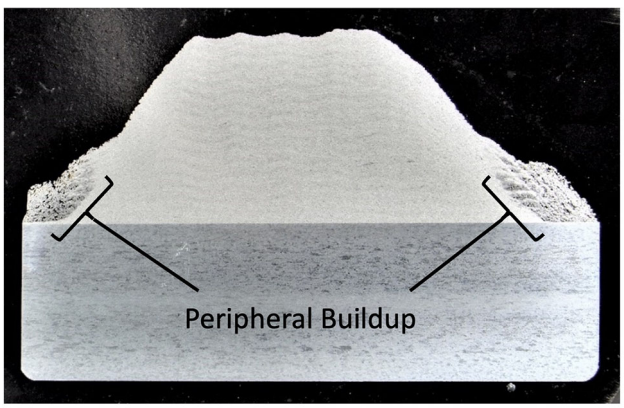

Fig. 9 Physical cross section of a tall deposit showing peripheral buildup along the edges

Height" Sections. However, track width does not change with v_n, which is discussed further in "Spread Parameter" Section.

One important observation from Fig. 8 is that as overall height of the deposit increases, a greater and greater amount of extraneous material builds up at the base of the deposit edges. A physical cross section of a deposit with this "peripheral buildup" is shown in Fig. 9. The buildup is much less dense and possesses significant porosity, as compared to the main deposit material. In most cases, such material would likely be removed after spraying. The quantity of the peripheral buildup appears to be related to overall deposit height, and it may be a result of spraying on the highly sloped edges of the taller deposits. To the authors' knowledge, this phenomenon has not been

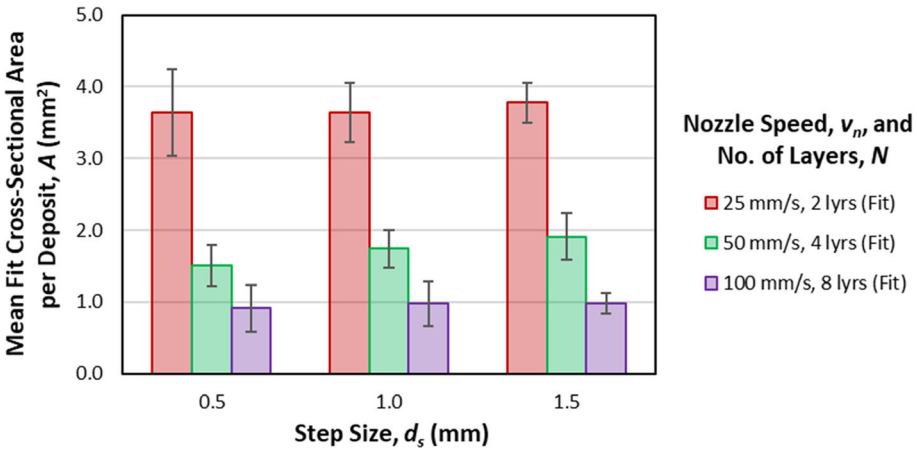

Fig. 10 Mean amplitude parameter, A, per track, averaged over all the tracks in each deposit

reported in the cold spray literature, to date. However, it has been observed during other sprays in the authors' laboratory, using low-density, high-ductility powders such as aluminum alloys. It is suspected that this is the buildup of smaller particles downstream that have been carried along with the jet as it deflected parallel to the sloped edges. However, further investigation is needed to confirm this.

Amplitude Parameter, A

The mean of the A values for each deposit is shown in Fig. 10 (corresponding values for each track are shown in Fig. 21 of the SI). As mentioned earlier, although A is not equivalent to cross-sectional area for large α, for the relatively small α values encountered in the present study, it is a close approximation. As qualitatively observed in Fig. 8 and 10 suggests that A is independent of step size, d_s, since, for a given v_n, the difference between values across d_s is statistically insignificant. This is an expected phenomenon, as A represents the amount of material deposited per unit length of a track, which should not depend upon the degree of track overlap. However, as will be shown shortly, there is a mild dependency of A on d_s, and it is the result of differing deposit surface morphologies between different step sizes.

While there is relatively weak relationship between A and d_s, a strong relationship between A and nozzle speed, v_n, is clearly present. As v_n is increased, A decreases, and vice versa. This observation is almost universally reported in the deposit shape literature (Ref 12, 15, 18), and it is simply a result of the fact that, at higher v_n, less material is deposited per unit length of a track. Empirical fits to A versus v_n are made in Fig. 11, for each step size, as well as all of the step sizes, combined. All of the trends are best fit by an inverse power law relationship:

$$A = C_A v_n^{-\beta_A} \quad \text{(Eq 5)}$$

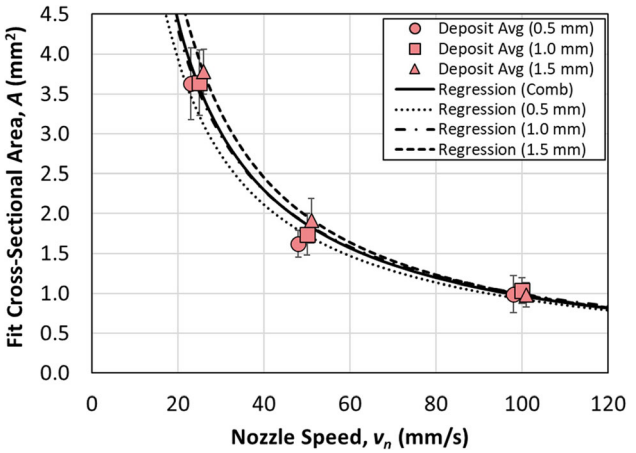

Fig. 11 Amplitude parameter, A, versus nozzle speed, v_n, for all nine deposits. Symbols represent the averages from Fig. 10; curves represent power law regressions to these datapoints

Table 3 Power law coefficients for Eq 5 from the regressions in Fig. 11

Step Size, d_s (mm)	C_A	β_A	R_A^2	DE (%)
0.5	57.7	0.897	0.988	55.0
1.0	65.9	0.911	0.993	62.8
1.5	96.2	0.995	0.999	91.7
Combined	73.8	0.941	0.987	70.3

Corresponding R^2 values are also listed, along with corresponding deposition efficiency, DE, values. The latter are discussed further below.

where C_A is a numerical coefficient and β_A is an exponent close to 1. The values for these coefficients (as well as R-squared values for the fits, R_A^2) are given in Table 3. It is noteworthy that there is a downward shift in the trendlines with decreasing step size, d_s. This is also indicated by the decreasing values of C_A in Table 3 with d_s, and it indicates

that the average track area becomes slightly smaller as step size becomes smaller. This is likely due to the fact that the deposit became narrower and taller as d_s was decreased, as a result of fixed the number of adjacent tracks per layer (8) in the present study. As a consequence, a larger portion of the deposit consisted of tall, sloped edges, resulting in an overall lower deposition efficiency. However, it is likely that, if the number of tracks per layer and number of layers were adjusted to result in equally tall and wide deposits, this phenomenon would be less pronounced or non-existent. As such the mild trend between A and d_s observed here is not an inherent relationship between track geometry and a nozzle path parameter, per se.

The value of C_A in Eq 5 is not universal but is particular to a given powder/substrate material combination and set of spray parameters (gas type, gas temperature, nozzle geometry, etc.). However, the near-unity value of β_A is, by contrast, somewhat general, and it is a result of the physics of the deposit buildup process. This is explained as follows. Let, at any given time, t, the mass accumulation rate of the deposit (d) material on the substrate be represented by $\dot{m}_\mathrm{d} = \partial m_\mathrm{d}/\partial t$. Furthermore, let ρ_d represent the mass density of the deposit material, $\dot{V}_\mathrm{d} = \partial V_\mathrm{d}/\partial t$ represent the volumetric deposition rate, A_tr represent the cross-sectional area of the track being laid down, and $v_n = \partial x_n/\partial t$ represent the nozzle traverse speed. Subsequently, the following relations for these quantities hold:

$$\dot{m}_\mathrm{d} = \frac{\partial m_\mathrm{d}}{\partial t} = \rho_\mathrm{d}\frac{\partial V_\mathrm{d}}{\partial t} = \rho_\mathrm{d}\dot{V}_\mathrm{d} = \rho_\mathrm{d}\frac{A_\mathrm{tr}\partial x_n}{\partial t} = \rho_\mathrm{d}A_\mathrm{tr}v_n \quad \text{(Eq 6)}$$

Rearranging the first and last terms gives

$$A_\mathrm{tr} = \left(\frac{\dot{m}_\mathrm{d}}{\rho_\mathrm{d}}\right)v_n^{-1} \quad \text{(Eq 7)}$$

The mass density of the deposit, ρ_d, is not, necessarily, equivalent to the mass density of the powder feedstock material, ρ, as porosity can be present in the deposit. Hence,

$$\rho_\mathrm{d} = (1-\phi_\mathrm{d})\rho \quad \text{(Eq 8)}$$

where ϕ_d is the porosity, with $0 \le \phi_\mathrm{d} \le 1$. Similarly, powder accumulation rate, $\dot{m}_\mathrm{d}$, is not, necessarily, equivalent to the powder mass feed rate, $\dot{m}_\mathrm{PFR}$, but is, instead, typically expressed as a function of the deposition efficiency, DE

$$\dot{m}_\mathrm{d} = \mathrm{DE}\cdot\dot{m}_\mathrm{PFR} \quad \text{(Eq 9)}$$

Powder feed rate is typically held constant during a spray, but deposition efficiency is a function of multiple parameters that are not always fixed. While the spray parameters (gas pressure, gas temperature, powder feeder gas flow rate, etc.) are typically fixed for a spray, the nozzle path parameters (standoff distance, angle, velocity, etc.) may not be. However, in the simple raster pattern sprays of the present study, any given track was specified by a fixed (v_n, d_s, N) combination, and all other nozzle path parameters were fixed, as well. The only variable that had an influence on DE was the slope of the underlying surface, which is a slight function of v_n. A slower nozzle speed builds a track with more sloped edges and a resulting lower deposition efficiency, and vice versa. This causes the coefficient, C_A, in Eq 5 to be a slight function of v_n, which is likely the reason that β_A is not exactly unity.

The form of Eq 7 has some validation in considering the behavior at the asymptotes. While not practically attainable, if v_n is theoretically increased indefinitely (i.e., approaching the horizontal asymptote at $v_n \to \infty$), the deposition rate, A, per unit time or length, should become infinitesimally small (i.e., $A \to 0$). Conversely, if v_n is decreased to zero (i.e., approaching the vertical asymptote), a deposit of theoretically infinite mass and size should accumulate (i.e., $A \to \infty$). In reality, these two limits are not practically achievable. An infinite v_n is not attainable, and a deposit will never exceed a certain, finite A, due to deposition efficiency eventually dropping to zero as a result of the eventual formation of highly sloped edges.

One consequence of the above development is that DE of an overall set of sprays can be estimated from the value for C_A obtained from an $A(v_n)$ fit. As mentioned above, the amplitude parameter for the skewed Gaussian fit for each track, A, is generally very close to the actual track cross-sectional area, A_{tr}, for the α values encountered in this study. Furthermore, since β_A is close to unity for all of the fits in the present study, the form of Eq 5 is sufficiently close to that of Eq 7 such that $C_A \approx \dot{m}_\mathrm{d}/\rho_\mathrm{d}$. Substituting Eq 8 and 9 into this and rearranging gives an expression for DE in terms of C_A and the deposit porosity, ϕ_d, powder mass density, ρ, and powder mass feed rate, $\dot{m}_\mathrm{PFR}$:

$$\mathrm{DE} \approx \frac{(1-\phi_d)\rho C_A}{\dot{m}_\mathrm{PFR}} \quad \text{(Eq 10)}$$

A use of Eq 10 is illustrated for the case of the fit to the combined step size results of Table 3. For Al 6061, ρ is 2.70×10^3 kg/m^3 (Ref 36), and, in the present study, $\dot{m}_\mathrm{PFR}$ was 8.5g/min. While ϕ_d was not measured in the present study, Julien, et al. (Ref 24) measured a value of 0.01% for Al 6061 deposits sprayed using identical parameters in a separate study. Finally, the value for C_A from the $A(v_n)$ fit was 73.8 mm^3/s. Since the tracks in this study represent the deposition of two consecutive tracks, the equivalent value of C_A for a single track is 36.9 mm^3/s. Substituting these

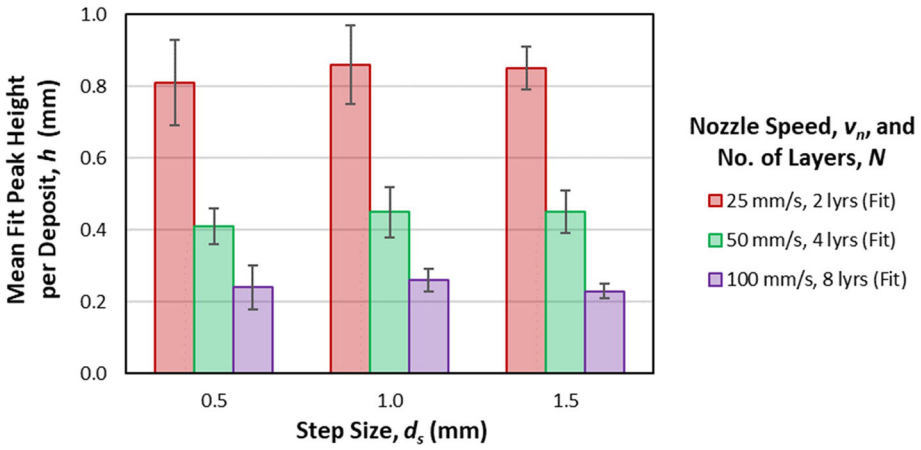

Fig. 12 Mean peak height, h, per track, averaged over all the tracks in each deposit

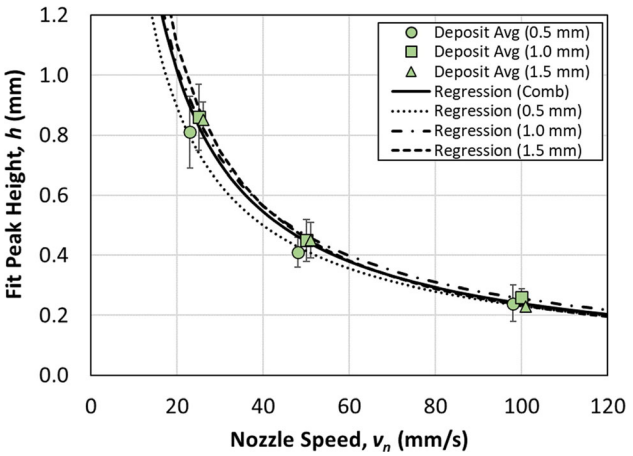

Fig. 13 Peak height, h, versus nozzle speed, v_n, for all nine deposits. Symbols represent the averages from Fig. 12; curves represent power law regressions to these datapoints

values into Eq 10 yields DE ≈ 70.3%. Values for DE were computed similarly for the individual step sizes in Table 3.

A theoretical value for DE can be computed using fit equations from computational fluid dynamics simulations that relate the particle velocity to the spray parameters (gas pressure and temperature, nozzle geometry, etc.) and powder properties (material, size distribution, etc.) (Ref 9). The deposition efficiency is estimated as the percentage of particles whose computed velocity exceeds the critical velocity at the location of the substrate, with the latter computed by the relation from Schmidt et al. (Ref 37). Using these relations and the parameters listed in Table 1, a theoretical deposition efficiency of 99.1% is obtained. In actual sprays, however, the value is often lower. For example, Story and Brewer (Ref 38) reported a DE of 71% for Al 6061 sprayed using helium at similar parameters as the present study (a VRC Gen III® cold spray unit at 3.2 MPa and 415 °C). Their sprays were conducted on a flat surface. In the present study, the even lower values for *DE* at the smaller step sizes is likely the result of spraying on the highly sloped edges of these deposits. Overall, therefore, the wide range of DE values listed in Table 3 is reasonable.

Table 4 Power law coefficients for Eq 11 from the regressions in Fig. 13

Step Size, d_s (mm)	C_h	β_h	R_h^2
0.5	11.04	0.840	0.997
1.0	13.60	0.863	0.998
1.5	19.70	0.963	0.999
Combined	14.77	0.894	0.992

Corresponding R^2 values are also listed.

While the DE estimated using the expression given in Eq 10 was comparable to a value reported in the literature, a comparison to direct measurement of DE by taking the ratio of feedstock mass deposited to feedstock mass sprayed would provide an improved validation of the proposed methodology. Such measurements will be reported in future work by the authors.

Peak Height, *h*

The mean peak height, h, values for each deposit are given in Fig. 12. Qualitatively, they exhibit similar trends to the mean values for A in Fig. 10: h is statistically invariant with respect to d_s but exhibits a strong dependence upon v_n. Empirical fits of h versus v_n are given in Fig. 13 for each step size and for all step sizes, combine. Similar to A, h also scales with v_n according to a near-inverse relationship.

$$h = C_h v_n^{-\beta_h} \qquad \text{(Eq 11)}$$

Best-fit values for the coefficients in Eq 11 are given in Table 4. Qualitatively, an apparent inverse relationship between h and v_n can be observed by Kotoban et al. (Ref 12), although empirical fits were not computed in that work.

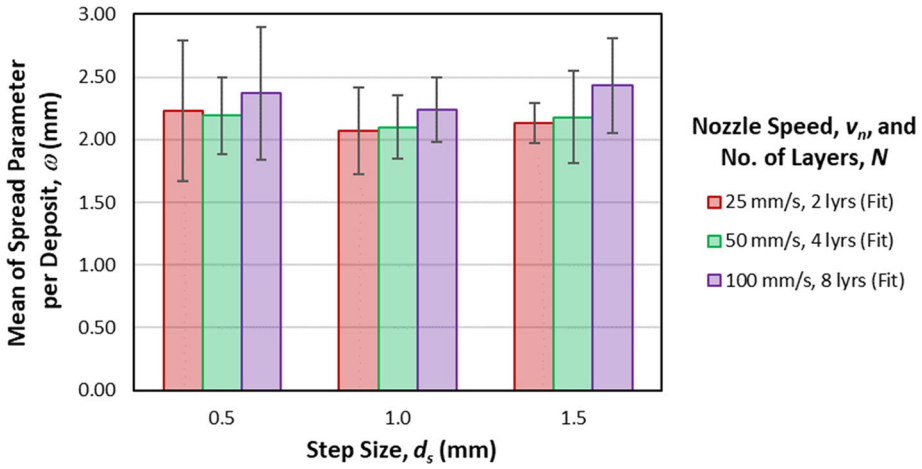

Fig. 14 Mean spread parameter, ω, per track, averaged over all the tracks in each deposit

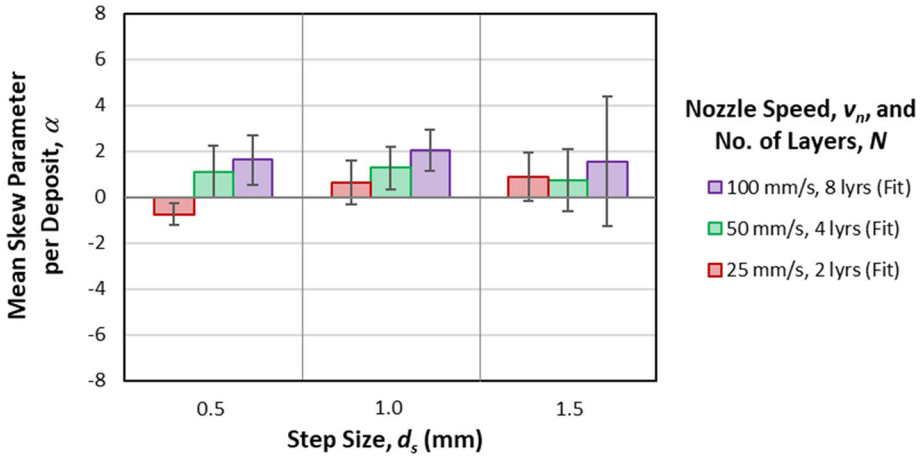

Fig. 15 Mean skew parameter, α, per track, averaged over all the tracks in each deposit.

Among the fits for each step size in Fig. 13, h exhibits a slight a downward shift in the trendlines with decreasing step size, d_s, similar to the trend observed for A versus d_s in Fig. 11. Although the trend is not distinct between the 1.5- and 1.0-mm step sizes, it is for the 0.5-mm step size. This decrease in average track height with shorter step size likely has the same cause as the decrease in A with d_s (c.f. "Amplitude Parameter" Section) and is, therefore, not an inherent relationship between h and d_s.

The reason for the close relationship between A and h is that the two are closely coupled for a skewed Gaussian distribution. For a standard Gaussian distribution, (1), it can be shown (c.f. Appendix 1) that the two are related by exactly,

$$h_{\text{std}} = \frac{A(v_n)}{\sqrt{2\pi}\sigma} \qquad \text{(Eq 12)}$$

For a skewed Gaussian distribution, a closed-form relationship cannot be obtained, but it can be shown that,

$$h_{\text{skew}} = \frac{A(v_n)}{\sqrt{2\pi}\omega} f(\alpha) \qquad \text{(Eq 13)}$$

where $f(\alpha)$ is a proportionality that is a function only of α (c.f. Appendix 2). Since, as will be shown shortly ("Skew Parameter" Section), ω is independent of v_n and α only varies mildly with it, the quantity $f(\alpha)/\sqrt{2\pi}\omega$ can be treated as nearly a constant, yielding the approximate relation $h_{\text{skew}} \propto A(v_n)$.

Spread Parameter, ω

The mean ω value for each deposit is shown in Fig. 14. Overall, ω does not vary significantly with either d_s or v_n. If ω is treated as a measure of track width, constancy with respect to d_s is rational, as track width would not be expected to change with the degree of overlap between tracks (barring changes in deposition efficiency due to spraying on highly sloped tracks). Constant track width with respect v_n is qualitatively observable in the experimental measurements work of Chen et al. (Ref 15) and Kotoban et al. (Ref 12). Indeed, most studies that model the shape buildup process treat track width as constant with respect to d_s and v_n (Ref 15, 17, 18, 20). The overall mean

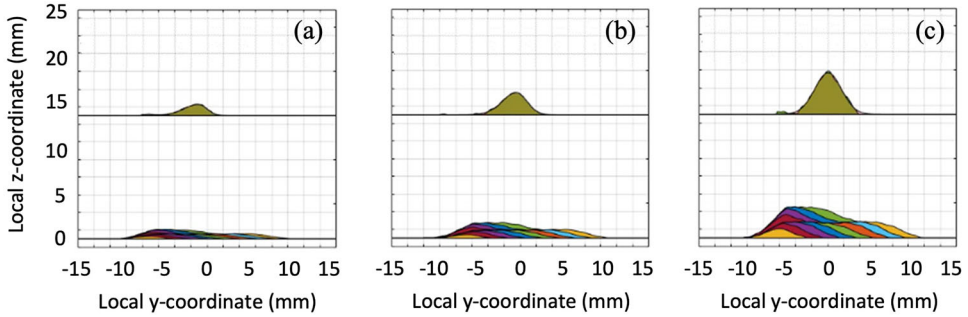

Fig. 16 Trend of decreasing α with decreasing v_n(c.f. Fig. 15), shown for Layer 2, Track 2 of the 1.0-mm deposits: (a) 100 mm/s ($\alpha = 2.48$), (b) 50 mm/s ($\alpha = 1.55$), and (c) 25 mm/s ($\alpha = 0.51$)

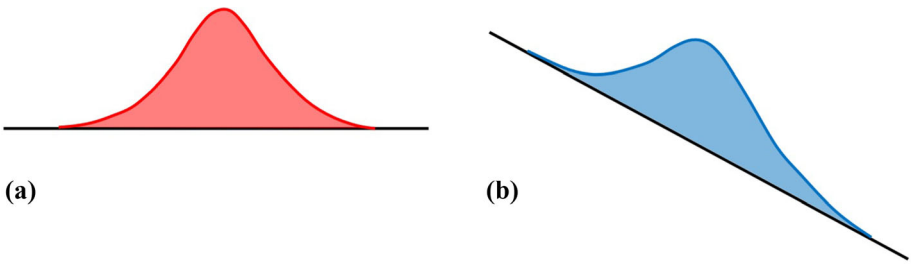

Fig. 17 Illustration of skew caused by spraying a track on a sloped surface: (a) an initially symmetric (simplified) Gaussian track sprayed normal to a horizontal surface; (b) a leftward skew induced spraying the same track on a surface with a left-to-right downward slope

value for ω across all the deposits in Fig. 14 is 2.26 ± 0.36mm.

Skew Parameter, α

The mean skew parameter, α, value for each deposit is shown in Fig. 15. Interestingly, with the exception of the 25-mm/s, 0.5-mm deposit, all of the deposits are biased with a slightly positive α value. This corresponds to a slight rightward skew. Observation of the first (left-most) track in the 25-mm/s, 0.5-mm, two-layer deposit in Fig. 3(c) shows a slight asymmetry to the track. Closeup observation of the shape of the first track in each deposit in Fig. 8 (closeups not shown) confirms that this asymmetry is consistent throughout the deposits.

In Fig. 15, α is largely independent of d_s but depends on v_n, with α decreasing slightly as v_n is decreased. The trend can also be qualitatively observed in the track cross sections in Fig. 16. This is attributed to two competing effects: (i) an inherent skew caused by the side-injection applicator, and (ii) a skew induced by spraying on a sloped underlying surface. The former effect is a result of the fact that the accelerating gas inlet on the applicator is positioned on the side of the applicator body, rather than coaxial with the nozzle and carrier gas inlet (c.f. Appendix 3). The latter effect is the result of a "counterbalancing" leftward skew caused by spraying each track on the slightly sloped underlying surface (e.g., Fig. 8). The schematic depiction of spraying on a sloped surface (Fig. 17) shows the track to take on a leftward skew (negative α), which is expected to become more pronounced (decreasing α) as the surface becomes more sloped. This was also demonstrated by Chen et al. (Ref 15), Wu et al. (Ref 17), and Li et al. (Ref 30). Thus, this skew counterbalances the inherent rightward skew (positive α) caused by the side-injection applicator. Since tracks sprayed at slower speeds are taller and have a greater slope, the resulting greater leftward skew (negative α) counterbalances the rightward skew (positive α) from the applicator, resulting in an overall reduced positive α value.

General Remarks

The flexibility of the skewed Gaussian distribution to represent asymmetric track cross sections can enable improved two-dimensional modeling of deposit cross-section buildup over the standard Gaussian distribution. An inherent track skew—such as caused by a side-injection applicator as in the present study—can be incorporated into simulation code via the skewed Gaussian distribution. Skew due to spraying at non-normal spraying angles could also be factored in. In the latter case, one would expect the parameters A, h, ω, and α to not only depend on d_s and v_n but also on the relative angle between the nozzle and the underlying surface, θ. Via a fairly straightforward set of experiments, the variation of these parameters with θ could be characterized, and the skewed Gaussian distribution could be incorporated into simulation code along with these relationships. This would provide a simpler alternative to the approach currently reported in the literature: skewing a symmetric input distribution using a projection of rays from the nozzle tip (Ref

15, 17, 30). The authors plan to extend the present work to different spray angles in the future.

To the authors' knowledge, the present study is the first in the cold spray literature to report a successful in situ deposit shape measurement methodology. While the total thickness of the deposits in the present study was approximately 3 to 5 mm, the method can be used to measure deposits of less than 1 mm in thickness. The thickness per layer in the present study varied between approximately 0.4 mm and 3 mm, depending upon the nozzle traverse speed and step size (with $(v_n, d_s) = (100\text{mm/s}, 1.5\text{ mm})$ and $(25\text{mm/s}, 0.5\text{ mm})$ for these two limits, respectively). For thin deposits, the main limit on thickness is imposed by the uncertainty in measurement in the vertical direction. While the profilometer has a vertical resolution of $\pm 0.4\mu m$ (c.f. Section 2.2), the vibration of the mount assembly during spraying resulted in a variation in measured height of approximately ± 0.2 mm (c.f. Section 2.4). Therefore, this is the theoretical minimum thickness that can be measured with the present system (for a relative uncertainty of $\pm 100\%$). Greater thicknesses would be needed if a lower relative uncertainty is desired. Improvement in the measurement accuracy could perhaps be obtained by reducing the sensor vibration during spraying or applying post-process data filtering. However, for many additive manufacturing applications of cold spray, greater thicknesses per layer are typically applied.

While, in the current study, the data were recorded during spraying, and the shape parameters were computed via post-processing, the present approach can be extended to measuring the shape and computing the shape parameters in real time. This would allow shape measurement to serve as a process monitoring tool. Changes in deposition rate—as a result, for example, of changes in gas parameters (temperature, pressure, or flow rate), nozzle path parameters (e.g., nozzle speed), or spray parameters (e.g., powder feed rate)—could be detected, in real time, and corrected. Nozzle angle could be adjusted, in real time, to optimize deposition efficiency or track shape. Furthermore, an inherent skew in track shape due to asymmetric applicator design could be compensated for by adjusting spray angle. Conceivably, spray system health—such as whether or not the nozzle or applicator is clogging—could also be monitored by monitoring track shape symmetry or deposition rate (track cross-sectional area).

Conclusions

In this work, a method has been presented by which the growing shape of a cold spray deposit can be studied on a track-by-track basis, using nozzle-tracking in situ laser profilometry. Furthermore, a skewed Gaussian distribution, rather than the typical symmetric Gaussian distribution, has been shown to better fit the shape of tracks when they are asymmetric. The fit parameters of the skewed distribution—such as amplitude parameter, A, peak height, h, spread parameter, ω, and skew parameter, α—can be used to study the shape of the tracks in relation to nozzle path parameters such as nozzle speed, v_n and step size, d_s. Many of these relationships,—such as that between amplitude parameter, A, and deposition efficiency, DE ("Amplitude Parameter" Section)—can be explained by physics-based arguments.

Table 5 Summary of relationships between track shape parameters and nozzle path parameters (I—inverse relationship; NR—no relationship)

	Nozzle path parameters	
	Nozzle speed,v_n	Step size, d_s
Track shape parameters		
Cross-Sectional Area,A	I	NR
Peak Height,h	I	NR
Spread Parameter,ω	NR	NR
Skew Parameter,α	I	NR

Table 5 summarizes those pairs of track shape and nozzle path parameters for which a significant relationship was found in the present study. While none of the parameters showed a strong correlation with step size, d_s, track cross-sectional area, A, and peak height, h, both showed a nearly inverse (I) relationship with nozzle speed, v_n, which was rooted in the physics of the mass accumulation rate of the material (c.f. "Amplitude Parameter" and "Peak Height" Sections). Spread parameter, ω, did not show a statistically significant relationship with v_n ("Spread Parameter" Section). However, skew parameter, α, showed an inverse (I) relationship, which had a physical basis in the slope of the underlying track ("Skew Parameter" Section).

To the authors' knowledge, the present study represents the first report of an in situ shape monitoring system in the cold spray literature. While the data, here, were recorded during spraying and then post-processed, the data processing and presentation can conceivably be extended to real time in a straightforward manner. Such a real-time shape monitoring approach would be of great aid in enabling cold spray to be applied to increasing complex additively manufactured parts. It is the authors' hope that the present work is a step in that direction.

Appendix 1: Derivation of Area and Height for a Standard Gaussian Distribution

The cross-sectional area of the standard Gaussian distribution given by Eq 1 can be obtained by integrating over its entire domain for y $(-\infty < y < \infty)$:

$$\text{Area} = \int_{-\infty}^{\infty} \frac{a}{\sqrt{2\pi}\sigma} \exp\left[-\left(\frac{y-\mu}{\sqrt{2}\sigma}\right)^2\right] dy = \frac{a}{\sqrt{2\pi}\sigma}\left[\frac{\sqrt{\pi}}{\sqrt{2}\sigma} Erf(y)\right]_{-\infty}^{\infty} = a \quad \text{(Eq 14)}$$

here it is observed that the area is equal to the value of the amplitude parameter, a.

The peak height of the standard Gaussian distribution given by Eq 1 can be obtained by computing the maximum z value of the distribution. By making the substitution of variables $p = (y-\mu)/(\sigma\sqrt{2})$, Equation 1 can be re-expressed as

$$z[p(y)] = \frac{a}{\sqrt{2\pi}\sigma} e^{-p^2} \quad \text{(Eq 15)}$$

Finding the local extremum by setting $\partial z/\partial y = 0$ yields

$$0 = \frac{a}{\sqrt{2\pi}\sigma} e^{-p^2} \frac{\partial p}{\partial y}(-2p) \quad \text{(Eq 16)}$$

Since the quantity before the parentheses never tends to 0 for finite y, the following is obtained.

$$0 = -2p \quad \text{(Eq 17)}$$

which is only true when $p = 0$. (Note that this is true when $y = \mu$.) Defining $h \equiv z[p = 0]$ yields Eq 12.

Appendix 2: Derivation of Area and Height for a Skewed Gaussian Distribution

Conceptually, the cross-sectional area of the skewed Gaussian distribution given by Eq 3 can be obtained by integrating over its entire domain for y $(-\infty < y < \infty)$:

$$\text{Area} = \int_{-\infty}^{\infty} \frac{A}{\sqrt{2\pi}\omega} \exp\left[-\left(\frac{y-\xi}{\sqrt{2}\omega}\right)^2\right]\left[1 + \text{erf}\left(\alpha\frac{y-\xi}{\sqrt{2}\omega}\right)\right] dy \quad \text{(Eq 18)}$$

However, a closed-form solution to this equation is not available for arbitrary α. Only when $\alpha = 0$ and Eq 3 reduces to (1) can a closed form expression be obtained. However, for the small α values encountered in the present study, A is numerically very close to the cross-sectional area of the distribution.

Conceptually, the peak height of a skewed Gaussian distribution represented by Eq 3 can be obtained by computing the maximum z value by setting $\partial z/\partial y = 0$. By making the substitution of variables $q = (y-\xi)/(\omega\sqrt{2})$, Eq 3 can be re-expressed as

$$z[q(y)] = \frac{A}{\sqrt{2\pi}\omega} e^{-q^2}[1 + \text{erf}(\alpha q)] \quad \text{(Eq 19)}$$

Taking the derivative $\partial z/\partial y$ and setting it equal to zero yields

$$0 = \frac{A}{\sqrt{2\pi}\omega} e^{-q^2} \frac{\partial q}{\partial y}\left\{(-2q)[1 + \text{erf}(\alpha q)] + \frac{2\alpha}{\sqrt{\pi}} e^{-(\alpha q)^2}\right\} \quad \text{(Eq 20)}$$

Since the quantity before the curly braces never tends to 0 for finite y, the following is obtained.

$$0 = -2q[1 + \text{erf}(\alpha q)] + \left(\frac{2\alpha}{\sqrt{\pi}}\right) e^{-(\alpha q)^2} \quad \text{(Eq 21)}$$

This expression does not have a closed-form solution and must be solved numerically for q. However, it is observed that q is implicitly a function of only α, $q = q(\alpha)$.

Observe that Eq 19 can be expressed as

$$z(y) = \frac{A}{\sqrt{2\pi}\omega} g(\alpha, q) \quad \text{(Eq 22)}$$

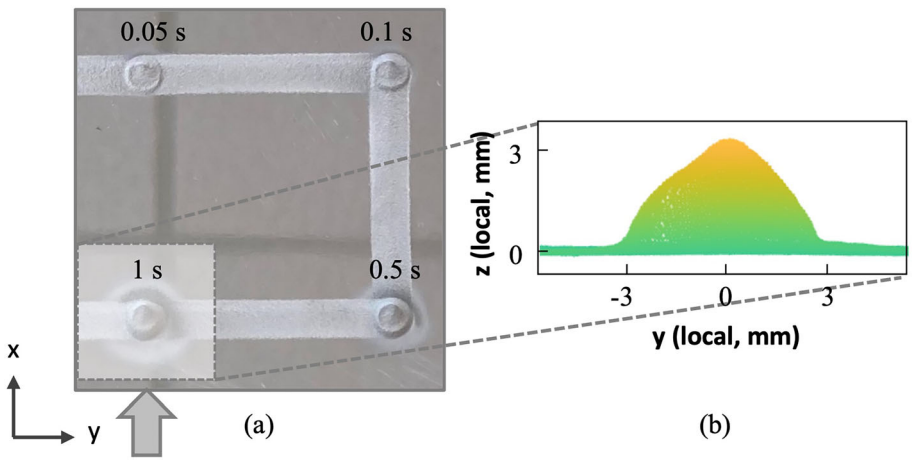

Fig. 18 (a) Array of single spot sprays, produced by holding nozzle position for the specified period of time. (b) Close-up of side-profile of the one-second spot, with viewpoint indicated by arrow in (a).

where $g(\alpha, q) = e^{-q^2}[1 + \mathrm{erf}(\alpha q)]$. The peak height of the distribution is, therefore, obtained by substituting the solution of Eq 21 into 22. Defining $f(\alpha) \equiv g[\alpha, q(\alpha)]$ gives Eq 13 in "Peak Height". Section.

Appendix 3 : Inherent Skew to Track Shape

A slight degree of asymmetry was both qualitatively observable (c.f. Section 3.2) and quantifiable ("Skew Parameter" Section) in the tracks of the present study. To better observe its nature, several spots were sprayed with the nozzle stationary for various periods of time (Fig. 18a). Qualitative observation of the spots showed that the peak was skewed significantly in the positive-x direction. In addition, scans by a 3D coordinate measurement machine ("CMM", Creaform® MetraSCAN BLACK, Lévis, Quebec, Canada) showed that there was slight asymmetry in the y–z plane (Fig. 18b). This skew is the result of the fact that the carrier gas inlet in the applicator used in the present study is located on the side of the applicator, rather than coaxial with the nozzle and powder carrier gas inlet. (To protect the commercial interests of the manufacturer, an image of the applicator is not shown here.)

Supplementary Information The online version contains supplementary material available at (https://doi.org/10.1007/s11666-024-01826-z).

Acknowledgements Funding for this work was provided, in part, by: the United States (US) Army Research Laboratory (ARL), award no. W911NF-20-2-0024; the National Institute of Standards and Technology (NIST), award no. 70NANB21H007; the Eaton Corporation; the US Army Corps of Engineers, Engineer Research and Development Center (ERDC), under OTA# W52P1J-20-93021; PPA CS-20-1201; and the National Center for Manufacturing Sciences (NCMS) and US Naval Sea Systems Command (NAVSEA), project no. 2021112-142136 under cooperative agreement HQ0034-15-2-0007. In addition, the authors would like to thank the following individuals at Northeastern University for their contributions: Daniel Akintola, Evelyn D'Elia, Jackson Hamilton, Katherine Liu, and Edward Oldak, who designed and built the hardware for the in situ profilometry system for their senior mechanical engineering capstone project; Tricia Schwartz, Jay Sanchez, for providing assistance and input on the sprays; and Theodore Lutkus, for optimizing the ROS coding for the in situ profilometer. The authors would also like to thank Robert Allegretto of VRC Metal Systems for providing assistance and technical guidance during the sprays. In addition, the authors would like to thank Charles ("Chuck") Simpson at Eaton, for conducting physical sectioning of several of the deposits.

Funding Open access funding provided by Northeastern University Library.

References

1. B. Hong, K. Wang, and P. Gu, Cold Spray-Based Additive Manufacturing of Thermosets, *J. Therm. Spray Technol.*, 2022, **31**(7), p 2003-2012. https://doi.org/10.1007/s11666-022-01428-7
2. Z. Khalkhali and J.P. Rothstein, Characterization of the Cold Spray Deposition of a Wide Variety of Polymeric Powders, *Surf. Coat. Technol.*, 2020, **383**, p 125251. https://doi.org/10.1016/j.surfcoat.2019.125251
3. J. Pattison, S. Celotto, R. Morgan, M. Bray, and W. O'Neill, Cold Gas dynamic Manufacturing: A Non-Thermal Approach to Freeform Fabrication, *Int. J. Mach. Tools Manuf.*, 2007, **47**(3), p 627-634. https://doi.org/10.1016/j.ijmachtools.2006.05.001
4. C. Li, Z.Y. Liu, X.Y. Fang, and Y.B. Guo, Residual Stress in Metal Additive Manufacturing, *Proc. CIRP*, 2018, **71**, p 348-353. https://doi.org/10.1016/j.procir.2018.05.039
5. H. Assadi, H. Kreye, F. Gärtner, and T. Klassen, Cold Spraying: A Materials Perspective, *Acta Mater.*, 2016, **116**, p 382-407. https://doi.org/10.1016/j.actamat.2016.06.034
6. K. Spencer, V. Luzin, N. Matthews, and M.X. Zhang, Residual Stresses in Cold Spray Al Coatings: The Effect of Alloying and of Process Parameters, *Surf. Coat. Technol.*, 2012, **206**(19), p 4249-4255. https://doi.org/10.1016/j.surfcoat.2012.04.034
7. V. Luzin, K. Spencer, M. Zhang, N. Matthews, J. Davis, and M. Saleh, Residual stresses in cold spray coatings, *Cold-Spray Coatings: Recent Trends and Future perspectives*. P. Cavaliere Ed., Springer International Publishing, Cham, 2018, p 451-480
8. L. He and M. Hassani, A Review of the Mechanical and Tribological Behavior of Cold Spray Metal Matrix Composites, *J. Therm. Spray Technol.*, 2020, **29**(7), p 1565-1608. https://doi.org/10.1007/s11666-020-01091-w
9. V.K. Champagne, O.C. Ozdemir, and A. Nardi, *Practical Cold Spray*, ed. (Cham, Switzerland, Springer, 2021).
10. K. Malamousi, K. Delibasis, B. Allcock, and S. Kamnis, Digital Transformation of Thermal and Cold Spray Processes with Emphasis on Machine Learning, *Surf. Coat. Technol.*, 2022, **433**, p 128138. https://doi.org/10.1016/j.surfcoat.2022.128138
11. M. Tzinava, K. Delibasis, and S. Kamnis, Self-organizing maps for optimized robotic trajectory planning applied to surface coating. in *Artificial Intelligence Applications and Innovations* (Cham, 2021), pp. 196-206
12. D. Kotoban, S. Grigoriev, A. Okunkova, and A. Sova, Influence of a Shape of Single Track on Deposition Efficiency of 316L Stainless Steel Powder in Cold Spray, *Surf. Coat. Technol.*, 2017, **309**, p 951-958. https://doi.org/10.1016/j.surfcoat.2016.10.052
13. M. Jeandin, F. Delloro, and M. Bunel, Advanced modeling and simulation tools to address build-up issues in additive manufacturing by cold spray, *Cold Spray in the Realm of Additive Manufacturing*. S. Pathak, G.C. Saha Ed., Springer International Publishing, Cham, 2020, p 129-175
14. M.M. Fasching, F.B. Prinz, and L.E. Weiss, Planning Robotic Trajectories for Thermal Spray Shape Deposition, *J. Therm. Spray Technol.*, 1993, **2**(1), p 45-57. https://doi.org/10.1007/BF02647423

15. C. Chen, Y. Xie, C. Verdy, H. Liao, and S. Deng, Modelling of Coating Thickness Distribution and Its Application in Offline Programming Software, *Surf. Coat. Technol.*, 2017, **318**, p 315-325. https://doi.org/10.1016/j.surfcoat.2016.10.044
16. D. Ikeuchi, A. Vargas-Uscategui, X. Wu, and P.C. King, Neural Network Modelling of Track Profile in Cold Spray Additive Manufacturing, *Materials*, 2019, **12**(17), p 2827.
17. H. Wu, X. Xie, M. Liu, C. Chen, H. Liao, Y. Zhang, and S. Deng, A New Approach to Simulate Coating Thickness in Cold Spray, *Surf. Coati. Technol.*, 2020, **382**, p 125151. https://doi.org/10.1016/j.surfcoat.2019.125151
18. H. Wu, X. Xie, M. Liu, C. Verdy, Y. Zhang, H. Liao, and S. Deng, Stable Layer-Building Strategy to Enhance Cold-Spray-Based Additive Manufacturing, *Addit. Manuf.*, 2020, **35**, p 101356. https://doi.org/10.1016/j.addma.2020.101356
19. C.V. Cojucaru, P. Vo, D. Levesque, C. Bescond, M. Rivard, J. Boisvert, G. Lamouche, M. Martin, and E. Irissou, Dimensional analysis and laser-ultrasonic inspection of cold spray additive manufacturing components, *Cold Spray in the Realm of Additive Manufacturing*. S. Pathak, G.C. Saha Ed., Springer International Publishing, Cham, 2020, p 219-244
20. Z. Cai, S. Deng, H. Liao, C. Zeng, and G. Montavon, The Effect of Spray Distance and Scanning Step on the Coating Thickness Uniformity in Cold Spray Process, *J. Therm. Spray Technol.*, 2014, **23**(3), p 354-362. https://doi.org/10.1007/s11666-013-0002-0
21. M. Tzinava, K. Delibasis, B. Allcock, and S. Kamnis, A General-Purpose Spray Coating Deposition Software Simulator, *Surf. Coat. Technol.*, 2020, **399**, p 126148. https://doi.org/10.1016/j.surfcoat.2020.126148
22. D. Ikeuchi, A. Vargas-Uscategui, X. Wu, and P.C. King, Data-Efficient Neural Network for Track Profile Modelling in Cold Spray Additive Manufacturing, *Appl. Sci.*, 2021, **11**(4), p 1654.
23. MIL-STD-32495A, Detail Specification, Powders for Cold Spray Deposition. Department of Defense (2018)
24. S.E. Julien, A. Nourian-Avval, W. Liang, T. Schwartz, O.C. Ozdemir, and S. Müftü, Bulk Fracture Anisotropy in Cold-Sprayed Al 6061 Deposits, *Eng. Fract. Mech.*, 2022, **263**, p 108301. https://doi.org/10.1016/j.engfracmech.2022.108301
25. J.P. Lynch, Robotic Assisted Cold Spray for Additive Manufacturing, Graduate Certificate in Engineering Leadership, Gordon Institute of Engineering Leadership (Northeastern University, Boston, Massachusetts, USA, 2020)
26. V. Champagne, A. Nardi, and D. Cote, Materials characterization of adavanced cold-spray aluminum alloys, *Int. J. Powder Metall.*, 2015, **51**(4), p 37-47.
27. K.S. Al-Hamdani, J.W. Murray, T. Hussain, and A.T. Clare, Heat-Treatment and Mechanical Properties of Cold-Sprayed High Strength Al Alloys from Satellited Feedstocks, *Surf. Coat. Technol.*, 2019, **374**, p 21-31. https://doi.org/10.1016/j.surfcoat.2019.05.043
28. V.K. Champagne, M.K. West, M. Reza Rokni, T. Curtis, V. Champagne, and B. McNally, Joining of Cast ZE41A Mg to Wrought 6061 Al by the Cold Spray Process and Friction Stir Welding, *J. Therm. Spray Technol.*, 2016, **25**(1), p 143-159. https://doi.org/10.1007/s11666-015-0301-8
29. J. Pattison, S. Celotto, A. Khan, and W. O'Neill, Standoff Distance and Bow Shock Phenomena in the Cold Spray Process, *Surf. Coat. Technol.*, 2008, **202**(8), p 1443-1454. https://doi.org/10.1016/j.surfcoat.2007.06.065
30. W. Li, H. Wu, M. Sokore, R.N. Raoelison, H. Liao, S. Costil, and S. Deng, General-Purpose Numerical Deposition Modeling Methodology Based on Mesh Geometry Reconstruction Strategy in Cold Spray Additive Manufacturing System, *Surf. Coat. Technol.*, 2023, **464**, p 129563. https://doi.org/10.1016/j.surfcoat.2023.129563
31. W.Y. Li, C. Zhang, X.P. Guo, G. Zhang, H.L. Liao, C.J. Li, and C. Coddet, Effect of Standoff Distance on Coating Deposition Characteristics in Cold Spraying, *Mater. Des.*, 2008, **29**(2), p 297-304. https://doi.org/10.1016/j.matdes.2007.02.005
32. J.L. Devore, *Probability and Statistics for Engineering and the Sciences*, 6th ed. Belmont, CA, USA: Thomson-Brooks/Cole (2004)
33. A. O'Hagan and T. Leonard, Bayes Estimation Subject to Uncertainty About Parameter Constraints, *Biometrika*, 1976, **63**(1), p 201-203. https://doi.org/10.2307/2335105
34. A. Azzalini, A Class of Distributions Which Includes the Normal Ones, *Scand. J. Stat.*, 1985, **12**(2), p 171-178.
35. S. Yin, P. Cavaliere, B. Aldwell, R. Jenkins, H. Liao, W. Li, and R. Lupoi, Cold Spray Additive Manufacturing and Repair: Fundamentals and Applications, *Addit. Manuf.*, 2018, **21**, p 628-650. https://doi.org/10.1016/j.addma.2018.04.017
36. ASM Handbook Volume 2A, *Aluminum Science and Technology*. Materials Park, (Ohio: ASM International, 2018)
37. T. Schmidt, F. Gärtner, H. Assadi, and H. Kreye, Development of a Generalized Parameter Window for Cold Spray Deposition, *Acta Mater.*, 2006, **54**(3), p 729-742. https://doi.org/10.1016/j.actamat.2005.10.005
38. W.A. Story and L.N. Brewer, Heat Treatment of Gas-Atomized Powders for Cold Spray Deposition, *Metall. Mater. Trans. A*, 2018, **49**(2), p 446-449. https://doi.org/10.1007/s11661-017-4428-8